Paper 86

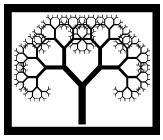

©Civil-Comp Press, 2012
Proceedings of the Eighth International Conference on Engineering Computational Technology, B.H.V. Topping, (Editor), Civil-Comp Press, Stirlingshire, Scotland

Mechano-Chemo-Electrical Finite Element Modelling of the Sensing Behaviour of Ionic Polymer Metal Composites

B. Akle[1], W. Habchi[1] and T. Wallmersperger[2]
[1] Department of Industrial and Mechanical Engineering
Lebanese American University, Byblos, Lebanon
[2] Institut für Festkörpermechanik, Technische Universität Dresden, Germany

Abstract

Ionic polymer metal composite (IPMC) is an electro-active polymer (EAP) that generates electrical charges when it is mechanically deformed. In this study, a fully-coupled mechano-chemo-electrical finite element model is developed to predict the velocity sensing behaviour in IPMC. The electro-chemical component is modelled based on the Nernst-Planck and Poisson's equations. The chemo-mechanical coupling arises from the change in the concentration of ions upon deforming the sensor. An experimental study is performed to validate the numerical model. The results are shown to be in good agreement with the model predictions.

Keywords: smart materials, electro-active polymers, sensor, finite elements, ionic polymer metal composite, ionic polymer transducers, multiphysics modelling.

1 Introduction

Smart materials are a class of materials that exhibit coupling between two or more physical domains [1]. Electromechanical transducers are a subset of smart materials that exhibit coupling between the electrical and mechanical domains as sensors or actuators. Electromechanically coupled polymers also known as electro-active polymers (EAP) are a soft and flexible class of transducers [2]. Ionic polymer metal composites (IPMCs) that are also known as ionic polymer transducers (IPTs) are derived from a relatively new class of electro-active materials with superior actuation and sensing capabilities [3-5]. As an actuator, IPMC exhibits bending strains up to 5% due to a 2V applied electrical potential across its electrodes [6]. In charge sensing mode, an IPMC sensor has been shown to be one order of magnitude more sensitive than traditional piezoelectric transducers [7,8]. In addition, IPMCs are reliable; IPMCs saturated with ionic-liquids have been shown to be environmentally stable and can operate over a million cycles in open air [9,10]. Further, these compliant sensors are suitable for conformal structures and based on

fabrication requirements they are cost competitive as compared to piezoceramic, MEMS, and other state-of-the-art sensors.
An IPMC is made of an ionomer film sandwiched between two conductive electrodes as shown in Figure 1. The commonly used ionomer in IPMC is Nafion, which is an acidic membrane containing covalently bonded negatively charged anions and positively charged cations. It is widely accepted that the motion of the cations is the main reason these smart materials are electro-mechanically coupled [11-16].

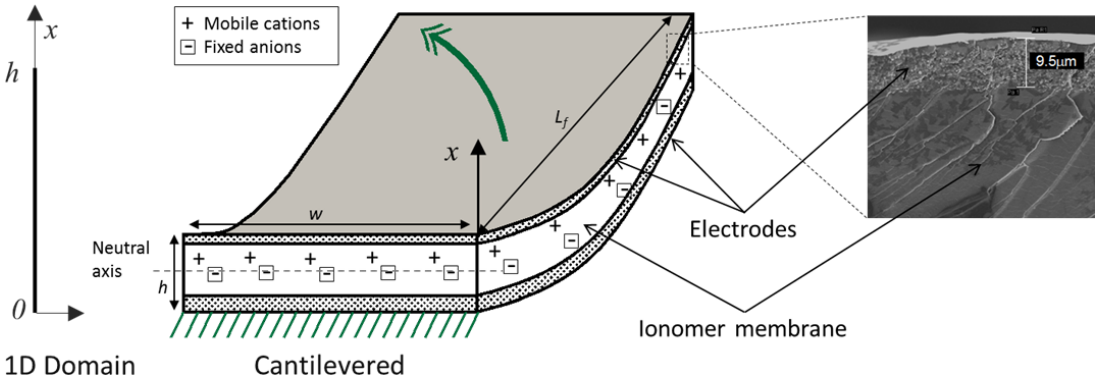

Figure 1 Schematic of an IPMC showing the high surface area electrode, the ionomer membrane, and the mobile cations. Also shown is a Scaning Electron Microscopy (SEM) image of the cross section of an IPMC, and the 1D representation. (the schematic is not to scale)

The primary reason this novel class of transducers has not been employed in high sensitivity applications is an inadequate understanding of the physics responsible for IPMC sensing. In this paper, the sensing response of IPMCs is studied and simulated. The purpose of such modelling efforts is to increase the understanding of the sensing mechanisms leading to an increase in its efficiency. Examples of sensing applications where effectiveness is highly dependent on the sensitivity of the measuring device include vibration control, health monitoring, and flow measurement [17].
This paper will start with a description of the model and the physics based hypothesis, followed by a brief experimental description. Numerical and experimental results are compared in the last section.

2 Model Description

Mechanical deformation of an ionic polymer produces ionic reorganization and conduction; this produces measurable electric charge flow. This is the basis for use of ionomeric materials as electromechanical sensors. Early ionomer research demonstrates that these films can be used as accelerometers for vibration sensing [3,4]. Shahinpoor et al. [5] summarize research in the use of ionomeric membranes as displacement and velocity sensors, primarily through the analysis and testing of

cantilever membranes. Their work quantifies the sensitivity of ionomeric materials under a variety of loading conditions.
More recently, the mechanical sensing properties of ionomers have been quantified and compared to that of piezoelectric films [7,8]. These works demonstrate that ionomeric films have excellent charge-sensing response when subjected to mechanical loads. Using a two-port impedance model of an ionomeric material, it is demonstrated that ionomeric films produce two to three orders of magnitude more charge than a piezoelectric film of equivalent size.
In order to develop the needed understanding of the physics of IPMC sensing, it is important to understand the composition of the ionomer material first. The ionomer widely used in IPMC is Nafion, which allows the positively charged cations to be mobile while the sulphuric negatively charged anions are fixed to the polymer matrix. The Nafion membrane is sandwiched between two electrically conductive electrodes. Upon bending the actuator, one side expands while the other contracts as it could be seen in Figure 1. The anion concentration increases at the inner compressed side of the sensor while it decreases at the outer expanded side.
The electrical, chemical and mechanical fields are assumed to be one-dimensional in the thickness direction *x* as the sensor's length and width are orders of magnitude larger than its thickness.
The multi-field model introduced in this paper describes the mechano-chemo-electrical behaviour inside an ionic polymer transducer. The formulation allows the computation of the space-time distribution of the electric potential and ionic concentration in the material for a given mechanical deformation.

2.1 Chemical Field

The formulation for the chemical field is based on the balance equation for the flux of the mobile ions and fixed charges. Using the conservation of mass and the Nernst-Planck equation for the flux, the convection-diffusion equation for each species reads:

$$\dot{c}_\alpha = \left[D_\alpha c_{\alpha,i} + z_\alpha c_\alpha \mu_\alpha \Psi_{,i} \right]_{,i} \qquad (1)$$

The variable c_α is the concentration of the species α while D_α is the diffusion constant, $\mu_\alpha = \frac{F}{RT} D_\alpha$ is the unsigned mobility, z_α is the valence of the ions, and Ψ is the electric potential. $\dot{c}_\alpha$ is the first derivative in time of the concentration c_α.

2.2 Electrical Field

The electric field is described by the quasi-static Poisson equation

$$\Psi_{,ii} = -\frac{F}{\varepsilon\varepsilon_0} \sum_{\alpha=1}^{N_f+N_b} \left(z_\alpha c_\alpha \right) \qquad (2)$$

where ε_0 is the permittivity of free space, ε is the relative dielectric constant, and F is the Faraday constant ($F = N_A \times e = 96487 C/mol$), where N_A is the Avogadro

constant and e is the electric elementary charge. N_f and N_b denote the number of freely movable species and the number of bound species, respectively.

2.3 Mechanical Field

The sensor in this study is in cantilever configuration and therefore the internal stresses due to a bending mechanical deformation are prescribed according to:

$$\epsilon = \epsilon_0(1 - 2x) \tag{3}$$

where ϵ is the strain and ϵ_0 is the maximum strain occurring on the electrodes. From classical beam theory [18], the maximum strain at the outer fibers could be calculated as follows:

$$\epsilon_0 = \frac{Md_h}{EI} \tag{4}$$

where M is the moment, d_h is the distance from the neutral axis, I is the second moment of area, and E is the modulus of elasticity. The sensor studied in this paper is symmetrical around the neutral axis and therefore $d_h = \frac{h}{2}$, where h is the thickness of the IPMC.

The mechanical and chemical domains are coupled by correlating the strain to the concentration of ions. For instance, the concentration of the negative ions that are bound to the polymer backbone is correlated to the strain using the following equation:

$$c^- = c_0^-(1 - \epsilon) \tag{5}$$

where c_0^- is the initial concentration of anions. The concentration of the positive cations (c^+) is considered initially to remain uniformly distributed throughout the domain resulting in the following equation:

$$c_0^+ = 1 \tag{6}$$

where c_0^+ is the initial concentration of cations. The assumptions of these equations is that during bending the concentration of the fixed anions increases in the contracting area while the mobile cations move with the diluent from the contracted area to the expanded areas to fill the voids.

2.4 Boundary Conditions at the Electrodes

In order to solve the given equations, boundary conditions for both the chemical and electrical field have to be specified. For the electric field, the electric potential is either prescribed at both domain boundaries or prescribed on one electrode and an electric field (gradient of the electric potential) is set to zero at the other electrode. The first condition simulates a short circuit current sensing configuration, while the second models a potential reading. For the chemical field, a zero-flux boundary condition ($J_i(x_i, t)=0$) is imposed over the polymer-electrode interface. This results in the following equation:

$$-D_\alpha c_{\alpha,i} - \frac{F}{RT} z_\alpha D_\alpha c_\alpha \Psi_{,i} = 0 \tag{7}$$

The electrical fields at the boundaries of the 1D domain is set to zero to simulate short circuit current sensing.

2.5 Non-Dimensional Analysis

The previously defined equations are all solved in their dimensionless form. This allows the use of a unique geometrical domain to represent different IPMC thicknesses. In addition, the different unknowns of the problem are scaled to the same order of magnitude providing a better conditioned system of equations. The different variables of the problem are scaled to unity by defining the dimensionless parameters:

$$\bar{x} = \frac{x}{h} \text{ and } \bar{c}_\alpha = \frac{c_\alpha}{c^-}$$

where h is defined as the thickness of an IPMC sensor (see Figure 1). The resulting dimensionless equations are:

$$h^2 \dot{\bar{c}}_\alpha = \left[D_\alpha \bar{c}_{\alpha,i} + z_\alpha \bar{c}_\alpha \mu_\alpha \Psi_{,i} \right]_{,i} \qquad (8)$$

$$\Psi_{,ii} = -h^2 c^- \frac{F}{\varepsilon \varepsilon_0} \sum_{\alpha=1}^{N_f+N_b} \left(z_\alpha \bar{c}_\alpha \right) \qquad (9)$$

and finally, the dimensionless boundary condition for the chemical problem is

$$-D_\alpha \bar{c}_{\alpha,i} - \frac{F}{RT} z_\alpha D_\alpha \bar{c}_\alpha \bar{\Psi}_{,i} = 0 \qquad (10)$$

2.6 Current Density and Charge Density

The ion transport in the polymer is directly related to the charge density (distribution):

$$\rho(\bar{x}_i, t) = F c^- \sum_{\alpha=1}^{N_f+N_b} (z_\alpha \bar{c}_\alpha(\bar{x}_i, t) \qquad (11)$$

The surface charge per unit area, $q^s(t)$, induced by the existence of a non-zero charge density ρ within the sample is obtained by an integration in the x-(thickness) direction

$$q^s(t) = \int_\Omega \rho x \, d\Omega \qquad (12)$$

The resulting current per unit area is the time derivative of the induced surface charge,

$$i(t) = \frac{dq^s(t)}{dt} \qquad (13)$$

The surface charge and current are computed using equations (12) and (13), respectively. The physical and geometrical parameters used in this study are shown in Table 1.

Parameter	Variable	Value
Polymer thickness	h	180 μm
Anion Concentration	c^-	1073 mol/m^3
Diffusion Coefficient	D_α	$6\cdot10^{-12}$ - $6\cdot10^{-10}$ m^2/s
Dielectric Constant	$\varepsilon\varepsilon_0$	$1.77\cdot10^{-4}$ - $1.77\cdot10^{-2}$ F/m
Temperature	T	293 K
Strain	$\in$	$1.7\cdot10^{-12}$ m/m

Table 1 Geometrical and Physical Parameters

3 Numerical Investigations

In this section the FEM model presented in section 2 is used to investigate the effect of the different physical parameters of IPMC on their sensing performance. First, the results of the charge distribution are presented throughout the thickness of the IPMC sensor, followed by a study of the effect of changing the dielectric constant (ε) and the diffusion constant (D_α) on the response of the IPMC sensor.

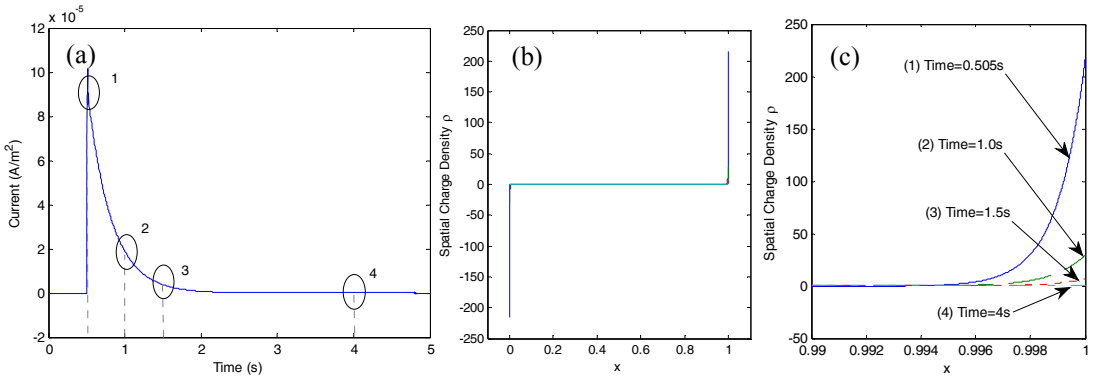

Figure 2 (a) The calculated short circuit current response due to a step input. (b) The charge density (ρ) across the thickness of the sensor while the step is applied. (c) A zoomed figure near the right electrode of the spatial charge density (ρ) at times in locations 1, 2, 3, and 4 of the step response.

First, the model is used to calculate the response due to a step strain input with the parameters shown in Table 1, and $\varepsilon = 1.77\bullet10^{-4}$ and $D_\alpha = 6\bullet10^{-11}$. Shown in Figure 2(a) is the short circuit current response. The known exponentially decaying response [7,8] of such sensors is clearly observed. The spatial charge across the thickness of the IPMC sensor is shown in Figure 2(b). It can be observed that a sharp boundary layer is formed at the electrodes. A similar behaviour is observed in actuated IPMC transducers [19,20]. Shown in Figure 2(c) is a zoomed response of the spatial charge density (ρ) near the right electrode at time locations 1, 2, 3, and 4 of the step response. Right after the application of the step response (at time t=0.505s), the boundary layer of the charge density is sharpest and decaying to

approximately zero when the decaying current reaches the steady state value of zero (time of more than 4s). The charge density becomes zero when the local concentration of positive and negative ions is the same (check equation 11). This is in-line with the proposed hypothesis that the imposed deformation perturbs the negative charges and the positive cations mobilize to achieve charge neutrality. The spatial charge density is symmetrical around the centre point and therefore a zoom in on the left electrode is not shown in the Figures.

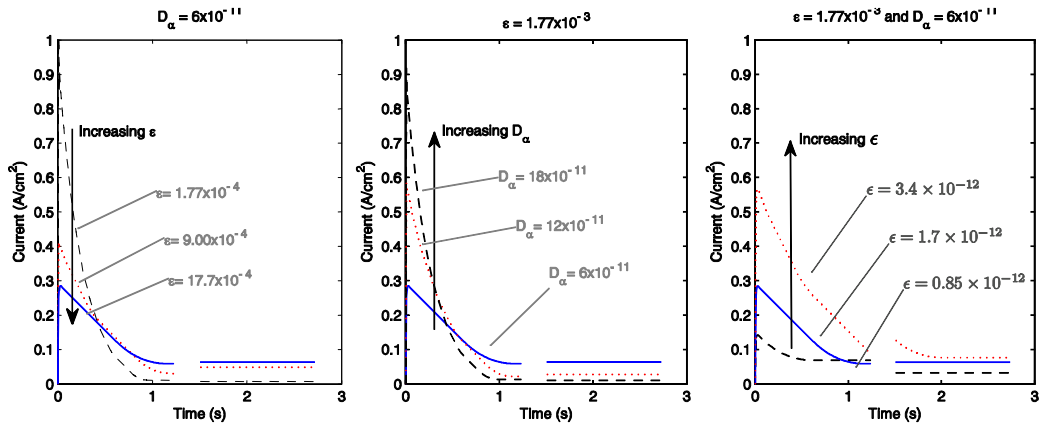

Figure 3 Short circuit current response due to a strain step input, (a) showing the effect of varying the dielectric constant (ε), while (b) shows the effect of increasing the diffusion coefficient (D_α), and (c) shows the effect of increasing the magnitude of the applied mechanical strain (ϵ).

First, a step response is simulated using the parameters shown in Table 1. Three parameters are varied: The diffusion coefficient (D_α), the dielectric constant (ε), and the mechanical strain (ϵ) which is the magnitude of the step. This study is performed to provide a calibration tool. For instance, it will provide the user with methods to increase the magnitude, the peak response, and the time constant. Shown in Figure 3(a) are three step responses with dielectric constant (ε) varying from $1.77 \bullet 10^{-4}$, $9.00 \bullet 10^{-4}$, and $17.7 \bullet 10^{-4}$ *(F/m)*; while the diffusion coefficient (D_α) and the mechanical strain (ϵ) are held constant at $6 \bullet 10^{-11}$ and $1.7 \bullet 10^{-12}$ respectively. The simulated results shown in Figure 3(a) and the calculated peak strain and time constant shown in Table 2 demonstrate that the peak current decreases with increasing dielectric constant, while the time constant increases. Shown in Figure 3(b) are three step responses with diffusion coefficient (D_α) varying from $6 \bullet 10^{-11}$, $12 \bullet 10^{-11}$, and $18 \bullet 10^{-11}$ *(m^2/s);* while the dielectric constant (ε) and the mechanical strain (ϵ) are held constant at $1.77 \bullet 10^{-3}$ and $1.7 \bullet 10^{-12}$ respectively. The simulated results shown in Figure 3(b) and the calculated peak strain and time constant shown in Table 2 demonstrate that the peak current increases with the dielectric constant, while the time constant decreases. The 37% time constant method is chosen to represent decay speed since the response is in the shape of an exponential function.

Diffusion Coefficient (D_α)	Dielectric constant (ε)	Mechanical Strain ($\in$)	Peak Current (A/cm^2)	Time Constant (s)
$6 \cdot 10^{-11}$	$1.77 \cdot 10^{-4}$	$1.7 \cdot 10^{-12}$	1.015	0.287
$6 \cdot 10^{-11}$	$9.00 \cdot 10^{-4}$	$1.7 \cdot 10^{-12}$	0.412	0.700
$6 \cdot 10^{-11}$	$1.77 \cdot 10^{-3}$	$1.7 \cdot 10^{-12}$	0.284	1.010
$6 \cdot 10^{-11}$	$1.77 \cdot 10^{-3}$	$1.7 \cdot 10^{-12}$	0.284	1.010
$12 \cdot 10^{-11}$	$1.77 \cdot 10^{-3}$	$1.7 \cdot 10^{-12}$	0.585	0.493
$18 \cdot 10^{-11}$	$1.77 \cdot 10^{-3}$	$1.7 \cdot 10^{-12}$	0.917	0.315
$6 \cdot 10^{-11}$	$1.77 \cdot 10^{-3}$	$0.85 \cdot 10^{-12}$	0.142	1.010
$6 \cdot 10^{-11}$	$1.77 \cdot 10^{-3}$	$1.7 \cdot 10^{-12}$	0.284	1.010
$6 \cdot 10^{-11}$	$1.77 \cdot 10^{-3}$	$3.4 \cdot 10^{-12}$	0.567	1.010

Table 2 The calculated Peak Current (A/cm^2) and the 37% Time Constant (s) as a function of the Diffusion Coefficient, Dielectric Constant, and Mechanical Strain

Finally, Figure 3(c) shows three step responses with varying mechanical strain ($\in$) from, $0.85 \cdot 10^{-12}$, $1.7 \cdot 10^{-12}$, and $3.4 \cdot 10^{-12}$ (m/m); while the dielectric constant (ε) and the diffusion coefficient (D_α) are held constant at $1.77 \cdot 10^{-3}$ and $6 \cdot 10^{-11}$ respectively. The simulated results shown in Figure 3(c) and the calculated peak strain and time constant shown in Table 2 demonstrate that the entire current response increases proportional to the strain, conserving the shape of the curve and hence the time constant.

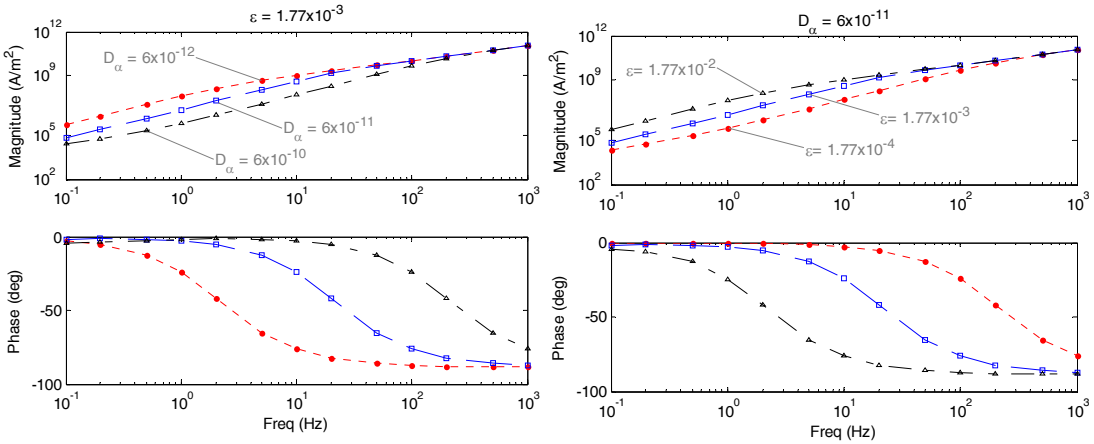

Figure 4 Frequency Response Functions generated from steady state sine responses showing both Magnitude and Phase Shift. (left) shows the effect of varying the Diffusion Coefficient (Dα), (right) the Dielectric Constant (ε)

In order to further understand the effects of varying the diffusion coefficient (D_α) and the dielectric constant (ε), a series of sine wave responses are simulated. For each sine wave response, the first 3 cycles are omitted and the magnitude and phase shifts are calculated from the remaining steady-state responses. The magnitude of the current per unit strain and phase shift is calculated from the fast Fourier transforms at the simulated frequency. Figure 4 (left) shows the effect of varying (D_α) on the FRF. It could be seen that the Magnitude at high frequencies is not

affected while it decreases with increasing (D_α) at the lower frequency. The phase demonstrates a phase shift of -90^o for all curves which is an indication of the presence of a real pole. The step response of a real pole is a decaying exponential which corresponds well to the simulation data presented earlier. Observed is the proportional increase in the frequency of the pole location as the diffusion coefficient is increased. This is also demonstrated in Table 3. This result indicates that the response of the IPMC becomes sensor is faster with increasing the diffusion coefficient. Figure 4 (right) shows the effect of increasing the Dielectric Constant (ε). Both the Figure and Table 3 demonstrate inversely proportional relationship between (ε) and the pole location. This leads to a conclusion that increasing (ε) slows down the system.

Diffusion Coefficient (D_α)	Dielectric constant (ε)	Pole Location (τ Hz)	Pole Location (τ rad/s)
$6\cdot10^{-11}$	$1.77\cdot10^{-4}$	223	1400
$6\cdot10^{-11}$	$1.77\cdot10^{-3}$	22.3	140
$6\cdot10^{-11}$	$1.77\cdot10^{-2}$	2.23	14
$6\cdot10^{-12}$	$1.77\cdot10^{-3}$	2.23	14
$6\cdot10^{-11}$	$1.77\cdot10^{-3}$	22.3	140
$6\cdot10^{-10}$	$1.77\cdot10^{-3}$	223	1400

Table 3 Pole location in both *Hz* and *rad/s* as a function of the Diffusion Coefficient (D_α) and the Dielectric Constant (ε)

4 Experimental Setup

In this section the experimental setup is presented. The IPMC sensor characterized here is fabricated using the Direct Assembly Process (DAP) described in Akle et al [21]. The ionomer is Nafion 117, the mobile cation in the sensor is Li^+, and the diluent is the EMI-TF ionic liquid, the 20μm electrodes are made from 42% vol RuO_2 high surface area particles.

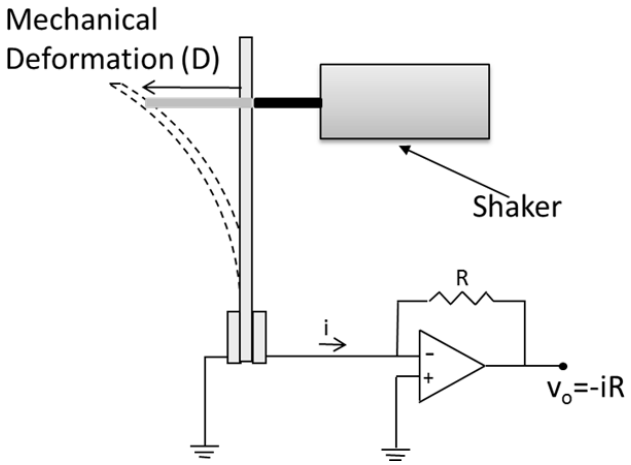

Figure 5 Schematic of the experimental setup detailing the electrical circuit.

The schematic of the experimental setup is shown in Figure 5. The setup is composed of an electromechanical shaker deforming the cantilevered IPMC sensor, and an electric circuit measuring the short circuit current that is generated by bending the IPMC. The dimensions of the characterized sensor are 28mm x 3mm x 0.25mm In order to normalize the deformation with respect to the shape of the IPMC sensor, the strain is calculated according to:

$$\epsilon = \frac{Dh}{L_f^2} \qquad (14)$$

where D is the measured tip displacement, h is the thickness of the IPMC sensor, and L_f is the free length of the cantilevered sensor (dimensions shown in Figure 1).

5 Experimental Results

In this section experimental data is measured and compared to results calculated from the numerical model. Furthermore, the model physical parameters are calibrated using the trends presented in section 3 to fit the time domain data in the form of step function, sine function and square wave function.

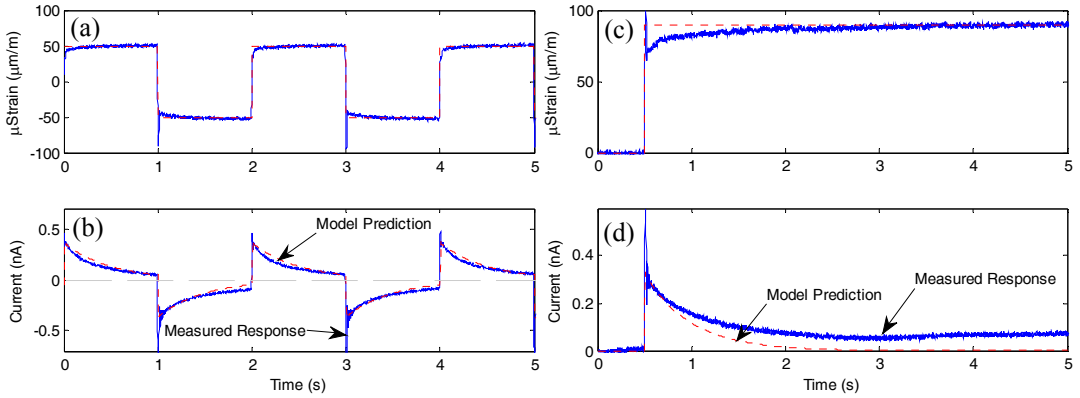

Figure 6 Measured experimental data compared to numerically simulated results: (a) square wave strain, (b) the square wave current response, (c) step strain, and (d) step current response.

The model is first calibrated with the square wave function as the measured strain is the closest especially on the positive side to a true square function. It is important to note that no feedback control algorithm is implemented on the applied strain, and the signal shape is applied to the electrical signal of the mechanical shaker in an open loop fashion. The resulting calibration parameters of the diffusion coefficient (D_α) and the dielectric constant (ε) are $9 \bullet 10^{-11} m^2/s$, and $1 \bullet 10^{-3} F/m$ respectively. Figure 6 (a) shows the applied strain as measured by the laser displacement sensor, along with the analytical square signal of frequency $1Hz$ applied to the numerical model. The current responses are shown in Figure 6(b) along with the calibrated model prediction. It could be observed that with the proper parameters the presented FEM model is able to predict well the response due to a square wave function. Next the

same calibrated parameters are retained and the model was simulated for a step input. The result is shown in Figures 6 (c) and (d) for the strain and current respectively. Comparing the numerical and the experimental currents one can conclude that the fit is fairly good, especially when considering the inaccurate shape of the applied strain as seen in Figure 6(c).

The model is again simulated with *1Hz* sine function while all the parameters are retained. Figures 7(a) and (b) show the resulting strain and current respectively. It could be observed that the measured current fairly matches the simulated results. Also notice that the measured response in both the strain and current sine waves are narrower in shape compared to the numerically simulated data. In an attempt to account for the distortion in the sine function, the measured strain curve is filtered using a 3rd order Butterworth low-pass filter with a cut-off frequency of *10Hz*, and used as input to the FEM model. The resulting simulation is again compared to the *1Hz* measured sine function in Figures 7(c) and (d) for the strain and current respectively. The numerical data is overlapping the experimental response much better especially on the positive side of the current.

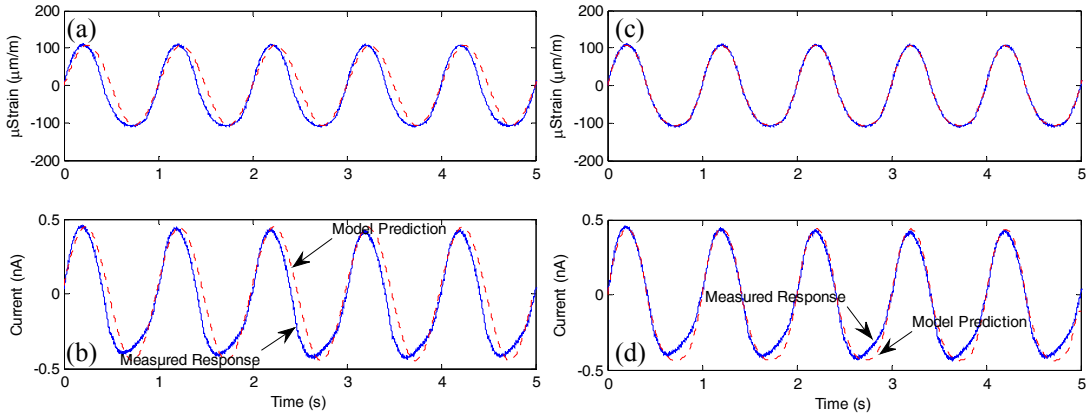

Figure 7 Measured experimental data compared to numerically simulated results: (a) sine wave strain, (b) the sine wave current response, (c) the filtered strain, and (d) corresponding current response.

Finally, a series of sine waves of frequencies 0.25Hz, 0.5Hz, 1Hz, 2Hz, 5Hz, and 10Hz are tested. Using Fast Fourier Transforms (FFT), the magnitude of the current per unit strain at all the tested frequencies is plotted in Frequency Response Function shown in Figure 8. It could be noticed that the magnitude increases quickly up to 2Hz and then followed by a slower increase. Compared to the numerically calculated response shown in Figure 4, the shape of the curves are very similar. The main discrepancy is the phase shift. In the simulated response the phase started at 0^o and ended at 90^o, as compared to a start at 90^o (interpolated) and an end of 180^o. The difference in phase shift is 90^o for both responses, with a difference of 90^o in start and end. The authors believe this is due to the signal conditioning circuit that is not accounted for in the numerical results. The IPMC sensor is a large capacitor which could form an RC type filter along with the current sensing circuit. Such filters could add or remove a 90^o phase shift.

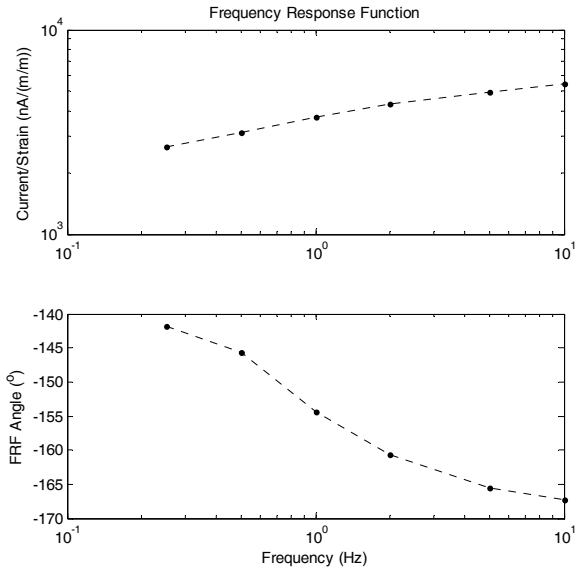

Figure 8 The Frequency Response Function of the measured current per unit strain.

6 Conclusion

This paper presents a finite element fully-coupled 1D mechano-chemo-electrical model for the sensing performance of IPMC . The electro-chemical component is modelled based on the Nernst-Planck and Poisson's equations. The chemo-mechanical coupling arises from the change in the concentration of ions upon deforming the sensor.

Manipulation of model parameters for a step input allowed the derivation of trends in the behaviour of the current response. For instance, increasing the diffusion coefficient (D_α) leads to an increase in the peak current and a decrease in the time constant; while an increase in the dielectric constant (ε) leads to a decrease in the peak current and an increase in the time constant; and finally an increase in the mechanical strain ($\in$) leads to an increase in both the peak current and the time constant. The effect of the same parameters is also assessed on the frequency response function. For instance; the model demonstrated that by increasing the dielectric constant (ε) leads to a decrease in the pole location; while increasing diffusion coefficient (D_α) leads to an increase in the pole location.

Experimental data in the form of steps, square wave, and sine wave are gathered and compared to the numerical results. The experiments proved to be in good agreement with the model predictions both in shape and magnitude. The results from the step response proved to be slightly off at steady-state. The sine wave experimental data matched well especially when the slightly distorted mechanical deformation was used as the input to the numerical model. Finally, an experimental FRF is obtained, and proved to be in agreement with the numerical simulation in its shape; while the phase was off by 90^o. The authors believe this arises because the signal conditioning circuit is not accounted for in the numerical results.

References

[1] D. J. Leo, “Engineering Analysis of Smart Material Systems”, John Wiley and Sons, New York, USA, 2007.

[2] Y. Bar-Cohen, ed., “Electroactive Polymer Actuators as Artificial Muscles”, SPIE Press, Bellingham, WA, USA, 2001.

[3] K. Oguro, Y. Kawami, H. Takenaka, “Bending of an ion-conducting polymer filmelectrode composite by an electrical stimulus at low voltage,” Journal of the Micromachine Society, vol. 5, pp. 27—30, 1992.

[4] K. Sadeghipour, R. Salomon, and S. Neogi, “Development of a novel electrochemically active membrane and 'smart' material based vibration sensor/damper”, Smart Mater. Struc. 1(2), 172, 1992.

[5] M. Shahinpoor, Y Bar-Cohen, J.O. Simpson, and J. Smith, “Ionic polymer-metal composites (IPMCs) as biomimetic sensors, actuators and artificial muscles - a review”, Smart Mater. Struct. 7(6), R15, 1998.

[6] B.J. Akle, D.J. Leo, “Single Walled Carbon Nanotubes - Ionic Polymer Electroactive Hybrid Transducers” Journal of Intelligent Material Systems and Structures, Vol. 19, No. 8, 905-915, 2008

[7] K. Newbury, D.J. Leo, “Electromechanical Modeling and Characterization of Ionic Polymer Benders,” Journal of Intelligent Material Systems and Structures, vol. 13, no. 1, pp. 51-60, 2002.

[8] K. Farinholt, D.J. Leo, “Modeling of electromechanical charge sensing in ionic polymer transducers," Mechanics of Materials, Volume 36, Number 5, pp. 421- 433(13), 2004.

[9] M. D. Bennett, and D. J. Leo, “Ionic liquids as stable solvents for ionic polymer transducers”, Sensors and Actuators A: Physical, 115(1), pages 79-90 2004.

[10] B. J. Akle, S. Nashwin, D.J. Leo, “Reliability of high-strain ionomeric polymer transducers fabricated using the novel direct assembly process”, Smart Mater. Struct. 16(2), 2007

[11] S. Nemat-Nasser, “Micromechanics of actuation of ionic polymer-metal composites”, J. Appl. Physics, 92(5), p. 2899-2915, 2002.

[12] S. Nemat-Nasser, and J.Y. Li, “Electromechanical response of ionic polymer-metal composites”, J. Appl. Phys., 87(7), p. 3321-3331, 2000.

[13] L.M, Weiland and D.J. Leo, “Computational Analysis of Ionic Polymer Cluster Energetics”, Journal of Applied Physics, 97, 013541, 2005.

[14] L.M, Weiland and D.J. Leo, “Ionic Polymer Cluster Energetics: Computational Analysis of Pendant Chain Stiffness and Charge Imbalance,” Journal of Applied Physics, 97, 123530, 2005.

[15] B.J. Akle, M.A. Hickner, D.J. Leo, and J.E. McGrath., “Correlation of capacitance and actuation in ionomeric polymer transducers”, Journal of Material Science, 40:3715–3724, 2005.

[16] C. Bonomo, L. Fortuna, P. Giannone, S. Graziani and S. Strazzeri, “A model for ionic polymer metal composites as sensors,” Smart Mater. Struct. 15, 749–758, 2006.

[17] G.J. Yun, K.A. Ogorzalek, S.J. Dyke, and W. Song, “A two-stage damage detection approach based on subset selection and genetic algorithms”, Smart Structures and Systems, 5(1), 1-21, 2009.
[18] J. E. Shigley, C. R. Mischke and Richard Budynas. “Mechanical Engineering. Design”, 7th Edition, McGraw-Hill, 2004.
[19] T. Wallmersperger, B. Akle, D.J. Leo, B. Kröplin “Electromechanical Response in Ionic Polymer Transducers: An Experimental and Theoretical Study”, Composite Science and Technology 68(5), S. 1173-1180, 2008
[20] B. Akle, W. Habchi, T. Wallmersperger, E. Akle and D. Leo, “High surface area electrodes in ionic polymer transducers: numerical and experimental investigations of the electro-chemical behavior” Journal of Applied Physics, 109(7), 074509, 2011.
[21] B. Akle, M. Bennett, D.J. Leo, K. B. Wiles and J.E. McGrath, “Direct assembly process: a novel fabrication technique for large strain ionic polymer transducers” Journal of Mat. Sci. Vol. 42, Number 16, pp. 7031-7041(11), 2007.